An International Journal
computers & mathematics with applications

PERGAMON Computers and Mathematics with Applications 46 (2003) 547–569

www.elsevier.com/locate/camwa

# Large-Eddy Simulation of a Reacting Scalar Mixing Layer with Arrhenius Chemistry

S. M. deBruynKops
Department of Mechanical and Industrial Engineering, University of Massachusetts
160 Governors Drive, Amherst, MA 01003-2210, U.S.A.
debk@ecs.umass.edu

J. J. Riley
Department of Mechanical Engineering, University of Washington
Box 352600, Seattle, WA 98195, U.S.A.

**Abstract**—A method for predicting filtered chemical species concentrations and filtered reaction rates in large-eddy simulations of nonpremixed, nonisothermal, turbulent reacting flows has been previously demonstrated to be quite accurate for higher Damköhler numbers and simple chemistry. The method extends quasi-steady flamelet concepts to model reactions that occur at lengths smaller than those resolved on the numerical grid. In this paper, the method is more fully tested using predictions of filtered mass fractions, temperatures, and reaction rates in an incompressible scalar mixing layer. One- and two-step reactions are considered, with activation temperatures and stoichiometric mixture fractions typical of reactions that occur in natural and engineering processes. The predictions for the mass fractions and temperatures are excellent in all cases considered for which quasi-steady flamelet modelling is appropriate. The predictions of the filtered reaction rates are also very good, even for cases where the reaction zones are very thin. Also demonstrated is a one-parameter model for the probability density of the subgrid-scale dissipation rate that significantly improves the predictions of the filtered reaction rates. 

**Keywords**—Large-eddy simulation, Turbulence modeling, Reacting flow, Nonpremixed.

## 1. INTRODUCTION

Accounting for chemical reactions in a large-eddy simulation (LES) requires knowledge of the distribution of reactants within each LES grid cell, and several approaches have been investigated by different researchers [1–8]. One aspect of the strategy investigated in this paper for accounting for subgrid-scale mixing is the utilization of an assumed form for the probability density function (PDF) of a conserved scalar within a grid volume. Gao and O'Brien [9] refer to this type of PDF as a large-eddy probability density function (LEPDF), while Colucci *et al.* [2] use the term filtered density function. Bilger [10] and Lentini [11] found that errors in assumed PDFs are greatly reduced upon integration, a common operation which is required in order to obtain, e.g., average or filtered concentrations. Frankel *et al.* [12] and Cook and Riley [13] demonstrated the

This work is supported by the National Science Foundation (Grant No. CTS9810103) and the Air Force Office of Scientific Research (Grant No. F49620-97-1-0092), and by grants of high performance computing (HPC) time from the Arctic Region Supercomputing Center. The authors benefitted greatly from discussions of this research with G. Kosály and J. Kramlich.

0898-1221/03/$ - see front matter  Typeset by AMS-TEX
doi: 10.1016/S0898-1221(03)00243-8

assumed LEPDF approach to be both practical and accurate for LES with equilibrium chemistry. In treating nonequilibrium chemistry, Frankel *et al.* [12] employed a joint Beta distribution for the fuel and oxidizer in a flow with a single-step reaction. Specification of the joint LEPDF requires modelling the subgrid-scale species covariance, a quantity that is very difficult to obtain accurately, although the using of a scaling model for the unmixedness shows promise [14]. An alternative method of accounting for nonequilibrium chemistry is to invoke the quasi-steady version of the flamelet approximation of Peters [15]. This approach, combined with Reynolds-averaged Navier-Stokes computations, has been recently applied to predict average species mass fractions in turbulent hydrogen-air flames [16–18]. The accurate predictions of laboratory data provide encouragement to apply the quasi-steady flamelet approach in the LES of turbulent combustion. To do so requires knowledge of the filtered dissipation rate and the subgrid-scale (SGS) variance of the scalar, quantities that potentially can be accurately modelled in an LES, since they are established by the large scales of motion.

Cook *et al.* [19] used flamelet theory, in conjunction with an assumed LEPDF, to derive a model for the filtered chemical species in an incompressible, isothermal flow with a single-step reaction. The model was termed the large-eddy laminar flamelet model (LELFM). Cook and Riley [20] extended the LELFM theory to the case of compressible flows with multistep, Arrhenius-rate chemistry. *A priori* tests of the model using data from direct numerical simulations (DNS) indicated that the LELFM is accurate, and improves with increasing Damköhler number. In the research reported in those papers, both the scalar subgrid-scale variance and filtered dissipation rate were computed directly by filtering data from the DNS.

The purpose of this paper is to present the results of integrated tests in which LELFM is used to predict filtered mass fractions, temperatures, and reaction rates directly from LES-simulated data. The benchmark against which the LELFM results are compared are direct numerical simulations (DNSs) of an incompressible reacting scalar mixing layer; the DNSs have been previously demonstrated to accurately represent the corresponding flow in wind tunnels for this case [21,22]. The chemical reactions include one-and two-step mechanisms with high activation temperatures and stoichiometric mixture fractions comparable to those of reactions that occur in natural and engineering processes.

## 2. MODEL FORMULATION

Numerical simulation of a constant density, reacting flow involves the discretization and numerical solution of conservation equations for mass, momentum, passive scalar, and in DNS, reacting scalar fields. When the conservation equations are discretized, length scales below those of the computational mesh spacing cannot be represented. In DNS, only flows are considered which would have negligible interaction between the resolved and the unresolved scales, and therefore, no modelling of the unresolved scales is required. In LES, the small scales are explicitly removed by applying a "grid filter" before the equations are discretized. The filter is defined by the convolution integral of the field being filtered $\phi$, and a filter kernel $g$, and the filtered quantity is here denoted with an overbar; i.e.,

$$\bar{\phi}(\vec{x}) \equiv \iiint_{-\infty}^{\infty} g(|\vec{x} - \vec{x}'|; \Delta)\, \phi(\vec{x}')\, d\vec{x}. \tag{1}$$

The filter kernel is normalized,

$$\int_{-\infty}^{\infty} g(r; \Delta)\, dr = 1, \tag{2}$$

and has a characteristic width $\Delta$ which is directly related to the grid spacing of the LES mesh. Applying the grid filter to the conservation equations removes information about the small scales, which must be added back into the simulations in the form of subgrid-scale (SGS) models.

### 2.1. Momentum and Conserved Scalar Transport

Piomelli [23] and Meneveau and Katz [24] review the current state of research into closure models for the momentum and passive scalar transport equations. The type of model needed in a particular LES depends on the complexity of the flow, the degree to which the large and small scales are in dynamic equilibrium, and the importance of the time history of the flow. In the simulations reported in this paper, turbulence undergoing isotropic decay with scalar mixing is considered, and the Smagorinsky model with dynamically computed coefficients [25–30] is adequate in capturing the large-scale features of the flow [31–34].

### 2.2. Reacting Scalars

The models for the unresolved terms in the momentum and conserved scalar equations rely on the fact that most of the kinetic and scalar energy resides in the largest scales. Thus, it is reasoned, a subgrid model need only extract the correct amount of energy from the large scales to be adequate for many applications. The same argument cannot be applied to be modelling of reacting scalars because, for moderate to high reaction rates, the scale of the entire flame lies below the grid scale. Hence, the chemistry model must be capable of approximating the interaction between the species within each LES grid cell. The large-eddy laminar flamelet model (LELFM) [19,20] is one approach to modelling the small scale structures. Although the model is applicable to compressible flows with multistep Arrhenius-rate chemistry [20], the derivation that follows assumes an incompressible flow since that is the subject of the current simulations.

Consider a two-feed combustion problem with fuel carried by feed 1 and oxidizer carried by feed 2. As the fuel and oxidizer are mixed, chemical reactions occur, forming combustion products. In this work, the reaction sets consists of one or more irreversible reactions of the form

$$\mathrm{A} + r\mathrm{B} \rightarrow (r+1)\mathrm{C}, \tag{3}$$

where $r$ is the mass of species B required to react with a unit mass of species A. A mixture-fraction $\xi(\vec{x},t)$ is defined, as in [10], so that, with the assumption of equal diffusivities of all species, $\xi$ is a passive conserved scalar in the flow, having a value of unity in feed 1 and a value of zero in feed 2.

In typical combustion problems, the zones of reaction are too small to be resolved by the LES; therefore, the chemistry must be modelled in its entirety. In deriving a model for the subgrid-scale chemistry, it is useful to note that the universal nature of the mixing of $\xi$ at the small scales of turbulence is well documented, supported by detailed laboratory experimental evidence, DNS data, and local solutions of the Navier-Stokes and scalar transport equations [35–38]. This motivates the use of flamelet theory in formulating a subgrid-scale model for the mass fraction of the $i^{\text{th}}$ species, $Y_i$.

Peters [15] proposed the following set of equations, derived from the species conservation equations, as a means of relating the species mass fraction $Y_i$ to the mixture-fraction $\xi$. These equations are expected to hold at high Damköhler numbers

$$-\frac{1}{2}\chi\frac{d^2Y_i}{d\xi^2} = \dot{w}_i, \qquad i = 1,\ldots,n, \tag{4}$$

where $\chi$ is the scalar dissipation rate, defined as

$$\chi \equiv 2D\frac{\partial\xi}{\partial x_j}\frac{\partial\xi}{\partial x_j}, \tag{5}$$

$n$ is the number of species in the reaction set, and $\dot{w}_i$ is the reaction rate of the $i^{\text{th}}$ species; the equation set is coupled through the reaction rates. Equation (4) satisfies the boundary conditions

$$Y_i = \begin{cases} Y_{i2}, & \xi = 0, \\ Y_{i1}, & \xi = 1, \end{cases} \tag{6}$$

where $Y_{i1}$ and $Y_{i2}$ are the uniform values of $Y_i$ in feeds 1 and 2, respectively. The dynamics of the local strain-diffusion competition involved in scalar mixing suggest that $\chi$ must be concentrated in locally one-dimensional, layer-like structures [15,35]. The $\xi$ dependence of $\chi$ is therefore prescribed as the solution to a one-dimensional, counterflow problem. The result is

$$\chi = \chi_0 F(\xi), \tag{7}$$

where

$$F(\xi) = \exp\left\{-2\left[\mathrm{erf}^{-1}(2\xi)\right]^2\right\}.$$

Here, $\chi_0$ represents the value of $\chi$ where $\xi = 0.5$, and $\mathrm{erf}^{-1}$ is the inverse error function (not the reciprocal).

### 2.2.1. Subgrid-scale PDF

By assuming that reactions occur in thin regions of one-dimensional counterflow, the $\xi$ dependence of $\chi$ is known through (7). In the modelling, it is assumed that $\chi_0$ is independent of $\xi$, so the average value of $Y_i$ within an LES grid cell can be expressed as

$$\bar{Y}_i = \int_0^1 \int_0^\infty Y_i(\xi, \chi_0) P(\chi_0) P(\xi)\, d\chi_0\, d\xi. \tag{8}$$

In (8), $P(\xi)$ is the LEPDF, giving the subgrid-scale probability density distribution of $\xi$ within the cell. Likewise, $P(\chi_0)$ gives the subgrid-scale probability density of $\chi_0$. To simplify notation, no distinction is made between the random variables and their probability space counterparts. Since the deviation between $Y_i$ and its equilibrium limit depends weakly on $\chi_0$ [16,39,40], it follows that

$$\bar{Y}_i = \int_0^1 Y_i\left(\xi, \bar{\chi}_0\right) P(\xi)\, d\xi. \tag{9}$$

The integral in (9) is carried out by assuming a Beta distribution for $P(\xi)$. Williams [41] gives this as

$$P(\xi) = \frac{\xi^{a-1}(1-\xi)^{b-1}}{B(a,b)}, \tag{10}$$

where

$$a = \bar{\xi}\left[\frac{\bar{\xi}\left(1-\bar{\xi}\right)}{\xi_v^2} - 1\right], \qquad b = \frac{a}{\bar{\xi}} - a,$$

$\xi_v^2 = \bar{\xi^2} - \bar{\xi}^2$ variance, as defined in (16) below, and $B(a,b)$ is the Beta function. Finally, $\bar{\chi}_0$ is related to $\bar{\chi}$ by integrating (7) with $P(\xi)$; i.e.,

$$\bar{\chi} = \bar{\chi}_0 \int_0^1 F(\xi) P(\xi)\, d\xi. \tag{11}$$

### 2.2.2. Filtered reaction rate

In the development of the LELFM, the instantaneous species mass fractions are written in terms of $\xi$ and $\chi_0$, in which case $T = T(\xi, \chi_0)$. Then, the filtered reaction rate for species $i$ is

$$\bar{\dot{w}}_i = \int_0^1 \int_0^\infty f_i[Y_1(\xi,\chi_0), Y_2(\xi,\chi_0), \ldots, Y_n(\xi,\chi_0)] \exp\left[\frac{-T_a}{T(\xi,\chi_0)}\right] P(\chi_0) P(\xi)\, d\chi_0\, d\xi, \tag{12}$$

assuming the PDFs of $\chi_0$ and $\xi$ are independent. Here, the Arrhenius term has been made explicit, and $f_i$ represents the functional relationship between the reaction rate of species $i$ and the mass fractions of all the species. In order to evaluate (12), a model for the $P(\chi_0)$ is required.

Cook [42], Cook and Riley [20], and de Bruyn Kops *et al.* [31] suggest replacing $P(\chi_0)$ with a delta function at $\bar{\chi}_0$, in which case (12) simplifies to

$$\tilde{w}_i \simeq \int_0^1 f\left[Y_1(\xi,\bar{\chi}_0), Y_2(\xi,\bar{\chi}_0), \ldots, Y_n(\xi,\bar{\chi}_0)\right] \exp\left[\frac{-T_a}{T(\xi,\bar{\chi}_0)}\right] P(\xi)\, d\xi. \tag{13}$$

Unfortunately, the approximation in (13) lacks the physical justification of that in (9).

An alternate approach for modelling $P(\chi_0)$ is to first note that the PDF of $\chi$ is approximately lognormal [43–47], and to surmise that the subgrid-scale PDF of $\chi$ will also be approximately lognormal since $\chi$ is dominated by the small scales. Next, as shown in [32], $P(\chi_0)$ is similar in form to $P(\chi)$, at least for the scalar fields considered in this research. Finally, Jiménez *et al.* [48] suggest a lognormal function with one parameter (the variance is proportional to the square of the mean) for approximating the PDF of $\chi$ conditioned on the mixture fraction, which motivates the following model for $P(\chi_0)$:

$$P(\chi_0) = \mathcal{L}(\chi_0; \bar{\chi}_0, a\bar{\chi}_0), \tag{14}$$

where $a$ is a constant of proportionality and the lognormal density function $\mathcal{L}$ is defined in terms of its mean $\eta$, and its standard deviation $\sigma$, as

$$\mathcal{L}(y;\eta,\sigma) = \frac{1}{\sigma\sqrt{2\pi}y} \exp\frac{-(\ln y - \eta)^2}{2\sigma^2}. \tag{15}$$

Since an LES is typically a simulation in which the majority of the scalar dissipation rate is in the subgrid-scale, the majority of the fluctuations in $\chi$ will occur at lengths smaller than the subgrid-scale for any size grid filter likely to be used. Therefore, the relationship between the SGS variance of $\chi$ and the local $\bar{\chi}$, if it exists, should not depend strongly on the grid filter width. This contrasts with the modelling of the SGS scalar variance since the majority of the fluctuations in $\xi$ are resolved, and the fraction that are unresolved depend strongly on the grid filter width.

### 2.3. Subgrid-Scale Mixing

The LELFM requires information about the SGS-mixing in the form of the SGS-variance $\xi_v^2$, and the filtered dissipation rate $\bar{\chi}$. Several models for each of these quantities have been previously examined [33,34], and the ones that were found to be most accurate are used here.

#### 2.3.1. SGS variance

The appropriate definition for the SGS variance in the context of a SGS PDF is [13,49]

$$\xi_v^2 \equiv \widetilde{\xi^2} - \tilde{\xi}^2. \tag{16}$$

This quantity can be modelled by relating it to the magnitude of the resolved scale gradient [42,50,51],

$$\xi_m^2 \equiv C_\xi \Delta^2 \left|\nabla\tilde{\xi}\right|^2. \tag{17}$$

The time-dependent coefficient $C_\xi$ is computed by assuming a form for the SGS scalar energy spectrum and adding it to the resolved-scale spectrum (from the LES) to form the complete scalar energy spectrum $E_\xi(k)$. Here, $k$ is the magnitude of the three-dimensional wave number vector. Next, a "test filter" with characteristic width larger than $\Delta$ is defined and denoted by $\widehat{(\,)}$. By assuming homogeneous turbulence, Cook [52] shows that

$$C_\xi = \frac{\displaystyle\int_0^\infty \left[1 - \tilde{g}^2(k;\Delta)\right] E_\xi(k)\, dk}{\displaystyle\int_0^\infty \left[1 - \tilde{h}^2\left(k;\hat{\Delta}\right)\right]\left[1 - \tilde{g}^2(k;\Delta)\right] E_\xi(k)\, dk}, \tag{18}$$

where $\tilde{g}$ and $\tilde{h}$ are the Fourier transformed grid and test filters, respectively. With $C_\xi$ computed from (18), the average SGS variance from (17) will exactly equal the average SGS variance implicit in $E_\xi(k)$, if the small-scale turbulence is isotropic [52].

In a high Reynolds number LES, the inertial range will extend to wave numbers which make an insignificant contribution to the SGS variance. If the grid filter is in the inertial range, it is reasonable to assume $E_\xi(k) \propto k^{-5/3}$ for all SGS $k$, and to ignore details of the spectrum in the dissipation range. In moderate Reynolds number flows, such as those presented in this work, the dissipation range accounts for a significant amount of the SGS variance and cannot be ignored. Therefore, a specific form for the high wave number spectrum is used which extends through the dissipation range [53–55]

$$E_\xi(k) \propto k^\alpha \exp\left(-\frac{3}{2} n D \varepsilon_T^{-1/3} k^{4/3}\right). \tag{19}$$

Pao [55] assigns the values $\alpha = -5/3$ and $n = 0.59$; for the moderate Reynolds number flows studied in this research, the values $\alpha = -1$ and $n = 1.2$ are used. While not needed to compute (18), the constant of proportionality in (19) may be determined by matching $E_\xi(k)$ to the actual LES spectrum at the highest resolved wave number. The kinetic energy flux supplied by the large eddies $\varepsilon_T$, can be estimated from the LES by assuming that it is equal to the energy removed from the resolved scales by the LES SGS model. Pao points out that the $\varepsilon_T$ used for the theoretical deduction of (19) (which assumes infinite Reynolds number) will always be greater than that measured in a laboratory experiment or, presumably, that computed from a LES of a flow with finite Reynolds number. Therefore, (19) is expected to underestimate the true SGS spectrum. While the effect that the error in $E_\xi$ will have on $\xi_m^2$ is not clear due to the application of the grid and test filters in (17), it is expected that $\langle \xi_m^2 \rangle \to \langle \xi_v^2 \rangle$ as the Reynolds number increases.

When the scalar field is homogeneous in at least one direction, the assumed spectrum method can be used by assuming homogeneity in the unresolved scales. In testing (19), Pao [55] notes that the longitudinal spectrum, $E_{\xi,1}(k_1)$, is related to $E_\xi(k)$ by [56]

$$E_{\xi,1}(k_1) = \int_{k_1}^{\infty} \frac{E_\xi(k)}{k}\, dk. \tag{20}$$

Following Pao's methodology, $E_\xi(k)$ is replaced by the assumed spectrum (19).

### 2.3.2. Filtered dissipation rate

Filtering the scalar energy equation results in the term

$$\bar{\chi} \equiv 2D\overline{\frac{\partial \xi}{\partial x_i}\frac{\partial \xi}{\partial x_i}} = 2D\overline{\frac{\partial \bar{\xi}}{\partial x_i}\frac{\partial \bar{\xi}}{\partial x_i}} + 2D\overline{\frac{\partial \xi'}{\partial x_i}\frac{\partial \xi'}{\partial x_i}} + 4D\overline{\frac{\partial \bar{\xi}}{\partial x_i}\frac{\partial \xi'}{\partial x_i}}, \tag{21}$$

which is the filtered dissipation rate. The first term on the RHS of (21) is the dissipation rate of $\bar{\xi}^2$, which can be computed directly from the resolved scales of an LES. The second term is the scalar dissipation rate caused by interaction among the small scales. The last term is due to interactions between resolved and unresolved scales, and can be either positive or negative. Girimaji and Zhou [57] develop models for the second and third terms and conclude that it is crucial that the backscatter (third) term be modelled accurately in an LES if $\bar{\chi}$ is to be computed accurately. In this work, however, $\bar{\chi}$ is used only as an input to the LELFM and not to close the transport equations for scalar energy in the LES; therefore, only the first term on the RHS of (21) is considered in the model for $\bar{\chi}$, which is defined as

$$\bar{\chi}_m \equiv C_\chi \overline{\frac{\partial \bar{\xi}}{\partial x_i}\frac{\partial \bar{\xi}}{\partial x_i}}, \tag{22}$$

where the constant $C_\chi$ is determined by assuming a form for the high wave number portion of the $\xi$ energy spectrum, e.g., (19), following Cook [58]. His analysis results in

$$C_\chi = \frac{\int_0^\infty k^2 E_\xi(k)\,dk}{\int_0^\infty k^2 \tilde{g}^2(k;\Delta) E_\xi(k)\,dk}. \tag{23}$$

In Section 2.3.1, it was argued that the assumed SGS $E_\xi(k)$ from (19) will always underestimate the true SGS spectrum because (19) was deduced for the case of infinite Reynolds number. While the effect of the error in $E_\xi(k)$ on $\xi_m^2$ is not obvious, it is clear that underpredicting $E_\xi(k)$ at high wave numbers will result in $\langle \bar{\chi}_m \rangle < \langle \bar{\chi} \rangle$. It is expected that $\langle \bar{\chi}_m \rangle \approx \langle \bar{\chi} \rangle$ for large enough Reynolds number.

## 3. REACTION MECHANISMS

Two reaction mechanisms with Arrhenius kinetics are considered in this research,

$$\mathrm{F} + r\mathrm{O} \rightarrow (1+r)\mathrm{P}, \tag{24}$$

and

$$\mathrm{A} + \mathrm{B} \rightarrow \mathrm{I} + \mathrm{C}, \tag{25}$$

$$\mathrm{B} + \mathrm{I} \rightarrow 2\mathrm{C}. \tag{26}$$

While the first mechanism is quite simple, it is examined over a wide range of parameters which result in reaction rates from near equilibrium to near extinction; it is also examined at a single Damköhler (defined below) but multiple Reynolds numbers. The second reaction set introduces the effects of free radicals and intermediate species. Details of each mechanism are given below.

### 3.1. Single-Step Mechanism

In the first mechanism, species O oxidizes species F in a single, irreversible step with the reaction rate of F given by

$$\dot{w}_\mathrm{F} = -A \exp\left(\frac{-\beta}{\alpha}\right) Y_\mathrm{F} Y_\mathrm{O} \exp\left[\frac{-\beta(1-T_r)}{1-\alpha(1-T_r)}\right]. \tag{27}$$

Here, $\alpha = (T_f - T_\infty)/T_f$, $\beta = \alpha T_a/T_f$, and $T_r = (T - T_\infty)/(T_f - T_\infty)$ [41]; $\alpha$ is a heat release factor, $\beta$ is a dimensionless activation energy, and $T_r$ is a reduced temperature equal to $Y_\mathrm{P}$. This formulation leads to a convenient definition of a global Damköhler number,

$$\mathrm{Da} \equiv \frac{AL}{u_{rms}} \exp\left(\frac{-\beta}{\alpha}\right). \tag{28}$$

A local Damköhler number, in which it is assumed that the local mixing-rate time scale is related to $\chi$, is

$$\mathrm{Da}_\chi \equiv \frac{A}{\chi} \exp\left(\frac{-\beta}{\alpha}\right). \tag{29}$$

This definition is intrinsic to the flamelet equation. In the case of high $\beta$, asymptotic methods can be used to derive a chemical time scale of the diffusion flame [59–61], which leads to a reduced Damköhler number defined at the stoichiometric surface

$$\mathrm{Da}_T \equiv \frac{rA\xi_{st} e^{-T_a/T_f}}{\chi_{st}/2} \left[\frac{T_f^2}{T_a(T_f-1)}\right]^3 [2\xi_{st}(1-\xi_{st})]^2. \tag{30}$$

### 3.2. Two-Step Mechanism

The second reaction mechanism used in this study is that developed by Swaminathan and Bilger [62] to model methane combustion by two reactions. Species A represents $CH_4$, B represents $O_2$, and I plays the role of the intermediate species $H_2$ and CO. Free radical appears as species R in the following rate expressions, which correspond to reactions (25) and (26), respectively:

$$\dot{w}_1 = -\left[A_1 \exp\left(\frac{-T_{a1}}{T_f}\right) T_f^{n_1} P\right] [1+\alpha(Y_T-1)]^{n_1} \exp\left(-\frac{\beta_1(1-Y_T)}{1+\alpha(Y_T-1)}\right) Y_A Y_R, \tag{31}$$

$$\dot{w}_2 = -\left[A_2 \exp\left(\frac{-T_{a2}}{T_f}\right) T_f^{n_2} P^2\right] [1+\alpha(Y_T-1)]^{n_2} \exp\left(-\frac{\beta_2(1-Y_T)}{1+\alpha(Y_T-1)}\right) Y_B Y_R. \tag{32}$$

The radical mass fraction is defined algebraically by

$$Y_R = K_R Y_I \sqrt{Y_B Y_I} \exp\left[-\lambda \sqrt{\frac{15}{4}} \frac{Y_A}{Y_B}\right]. \tag{33}$$

$Y_T$ is the temperature difference between the true temperature and the inlet stream temperature scaled by the specific heat at constant temperature, the heat release per mole of fuel, and the specific abundance of fuel species in the unmixed state; $Y_T \approx 0.3$ when $T = T_f = 2350\,\mathrm{K}$, the adiabatic flame temperature. The thermodynamic pressure, $P$, is taken to be unity. The global Damköhler numbers are defined as

$$\mathrm{Da}_i \equiv \frac{A_i L}{u_{rms}} \exp\left(\frac{-\beta_i}{\alpha}\right) T_f^{n_i} P, \qquad i = 1, 2. \tag{34}$$

The values of the remaining constants appearing in the rate equations are the same as those used in [62], $K_R = 1.477$, $\lambda = 0.5$, $T_{a1} = 5455\,\mathrm{K}$, $T_{a2} = 0\,\mathrm{K}$, $n_1 = 1.6$, $n_2 = -1.72$.

## 4. DESCRIPTION OF THE SIMULATIONS

The flow field considered in this research is a reacting scalar mixing layer in decaying grid turbulence. A schematic of the flow showing the one-step reaction is given in Figure 1. While temperature affects the rates of the chemical reactions, the velocity field is considered to be incompressible. The velocity and conserved scalar data from the direct numerical simulations [21,22] closely resemble those in the laboratory experiments of Ma and Warhaft [63], which, combined with spatial and temporal resolution tests, give confidence that the DNS data very nearly represent a canonical mixing layer and, therefore, provide a good benchmark against which to compare the LES results. Additional details concerning the accuracy of the simulations are presented in [22,34].

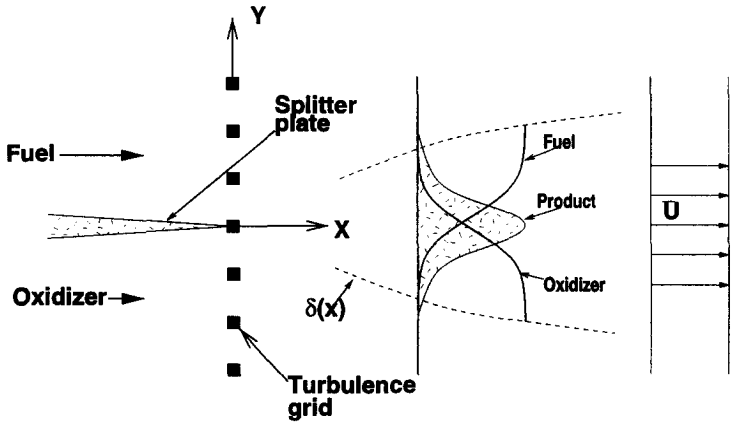


Figure 1. Schematic of a reacting mixing layer with a one-step reaction.

In the simulations, temporally decaying turbulence in a three-dimensional box is considered to be convected by the mean flow. The computational domains contain $512^3$ (DNS), $128^3$, and $64^3$ (LES) grid points and use periodic boundary conditions in the $x$ and $z$ directions and a free slip condition in the $y$ direction (the direction of the mean scalar gradient). The corresponding physical problem is a cube 25.1 cm on a side being convected by the mean flow downstream of a turbulence-generating mesh in a wind tunnel; downstream distances range from 25.4 to 231 times the spacing of the mesh.

The DNS method used in this research is the same as that used by de Bruyn Kops and Riley [64] to accurately simulate the decaying isotropic turbulence experiment of Comte-Bellot and Corrsin [65], and the large-eddy simulations employ the same code modified to include the SGS terms in the momentum and scalar transport equations. Briefly, a massively-parallel, pseudospectral code advances the transport equations in time, with all the large scales fully resolved, and the small scales either fully resolved (DNS) or modelled (LES). Pseudospectral Fourier methods are used to approximate spatial derivatives; these derivatives are computed in Fourier space and nonlinear algebraic terms are computed in real space. This pseudospectral method has the advantages that phase errors are very small, rates of convergence are very high, and the truncation error decreases faster than algebraically as the number of Fourier modes becomes large [66]. The method has been found to be twice as accurate as finite-difference schemes using the same resolution [67]. A second-order Adams-Bashforth scheme with projection is used for time-stepping.

Pseudospectral methods suffer from errors caused by the aliasing of energy at high wave numbers to lower wave numbers when nonlinear terms are computed in physical space. These aliasing errors can be eliminated by applying a spectral mask to remove energy in wave numbers greater than $N/3$, where $N$ is the number of grid points in each direction [68,69]. This is equivalent to applying a spectral truncation grid filter with $\Delta$ equal to 1.5 times the grid spacing. In LES using the Smagorinsky SGS model with a dynamically computed coefficient, it is especially important to eliminate aliasing errors to prevent them from being fed back into the calculation of the Smagorinsky coefficient. For this reason, the $N/3$ mask is used for all LES reported in this work. In DNS, sufficient dealiasing is achieved if the energy in wave numbers greater than $15N/32$ is removed [70]. The $15N/32$ mask is equivalent to a spectral truncation grid filter with $\Delta$ equal to 16/15 times the grid spacing. Such a grid filter is used in this work for DNS. For consistency, the LES test filter is also a spectral truncation filter with $\hat{\Delta} = 2\Delta$. The ratio of $\hat{\Delta}$ to $\Delta$ is based on *a priori* tests by Germano *et al.* [27].

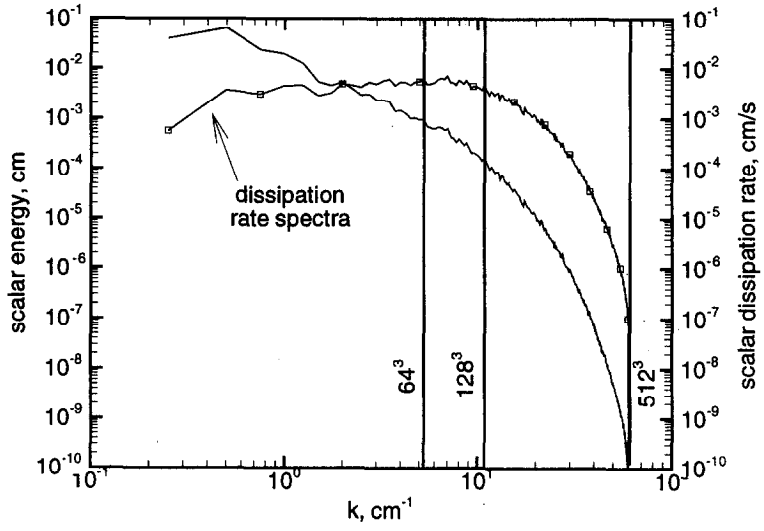


Figure 2. One-dimensional scalar energy and dissipation rate spectra on centerline at $x/M = 50.1$.

As an indication of the resolution of the scalar fields on the three numerical grids, the one-dimensional scalar energy and dissipation rate spectra on centerline at $x/M = 50.1$ are displayed in Figure 2. The fractions of scalar energy and dissipation rate that are accounted for by the resolved scales are given in Table 1. It is apparent from both the figure and the table that, in the large-eddy simulations, most of the scalar energy is resolved but that the significant scalar dissipation occurs at scales smaller than the grid scale and so must be modelled. With the $128^3$-point grid in the far field ($x/M = 231$), very little modelling of $\tilde{\chi}$ or $\xi_v^2$ is required; nevertheless, the reaction zones for the reactions considered are much smaller than either the mixing zone or the grid scale, and so considerable modelling is required to predict filtered mass fractions and dissipation rates.

Table 1. Fraction of scalar energy and dissipation rate accounted for by the resolved scales at different grid resolutions.

| Grid | $x/M$ | Energy Fraction | Dissipation Rate Fraction |
|---|---|---|---|
| $64^3$ | 50.1 | 0.95 | 0.30 |
| $64^3$ | 231 | 0.98 | 0.74 |
| $128^3$ | 50.1 | 0.99 | 0.68 |
| $128^3$ | 231 | 0.99 | 0.97 |

## 5. CHARACTERISTICS OF THE REACTIONS

Six chemistry cases are considered in this paper. These include a set of three single-step mechanisms in which all parameters are held constant except for the initial Damköhler number, a set of two single-step mechanisms in which only the stoichiometric ratio is varied, and a two-step mechanism. The reaction parameters are given in Tables 2 and 3. To provide an overview of the relative reaction rates and amount of extinction in the simulated one-step reactions, scatter plots of the product mass fractions ($Y_P$) versus the mixture fraction ($\xi$) are shown in Figure 3. Scatter plots of mass fractions and scaled temperature for the simulations involving a two-step reaction are given in Figure 4. The upper four panels in Figure 3 are for the three cases involving $F + rO \rightarrow P$ with $r = 1$ (ML3, ML4, ML5), with Case ML4 shown at two different downstream locations, and thus two different values of $\langle Da_T \rangle$. In Case ML3, there is considerable mixing without burning, either due to extinction or nonignition, and tests indicate that reducing Da by a factor of two from what it is in the ML3 case results in global extinction. In Case ML5, the reaction rate is about 17 times higher than it is in Case ML3; the reaction occurs at the equilibrium rate in most locations at $x/M = 50.1$ (shown), and at virtually all locations at $x/M = 231$ (not shown). Thus, Cases ML3 and ML5 bracket the full range of reaction rates from very low to near equilibrium. Figure 5 shows the unscaled profiles of the average product mass fraction for these two simulations. Both start with the same equilibrium chemistry condition, but the product advects and diffuses faster than it is created in Case ML3 while being created faster than it advects and diffuses in Case ML5.

Table 2. Reaction parameters for one-step reactions.

| | $\alpha$ | $\beta$ | $r$ | Da Initial | Da Final | $\langle Da_T \rangle$ at $x/M = 50.1$ | $n_r$ at $x/M = 50.1$ |
|---|---|---|---|---|---|---|---|
| ML3 | 0.88 | 5.4 | 1 | 17.8 | 215 | 0.79 | 26 |
| ML4 | 0.88 | 5.4 | 1 | 75.7 | 914 | 3.2 | 16 |
| ML5 | 0.88 | 5.4 | 1 | 302 | 3659 | 13.0 | 10 |
| ML6 | 0.88 | 2.6 | 10 | 53.6 | 647 | 4.3 | 14 |
| ML7 | 0.88 | 2.6 | 30 | 53.6 | 647 | 0.66 | 27 |

Table 3. Reaction parameters for two-step reactions.

| | $\alpha$ | $\beta_1$ | $\beta_2$ | $Da_1$ Initial | $Da_2$ Initial | $Da_1$ Final | $Da_2$ Final |
|---|---|---|---|---|---|---|---|
| ML8 | 0.62 | 1.4 | 0 | 17.2 | 1.12 | 207 | 13.5 |

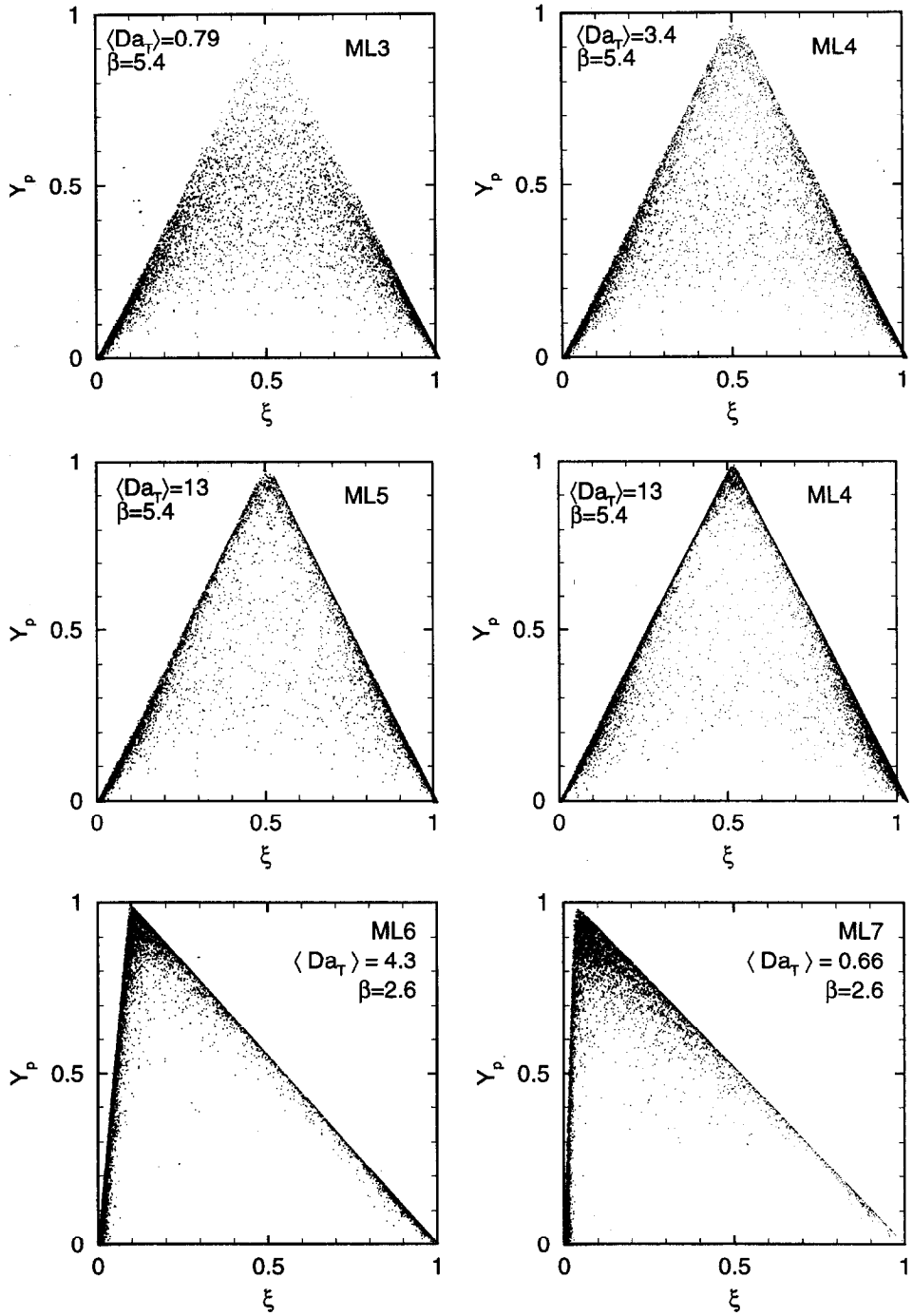


Figure 3. Scatter plots of $Y_P$ versus $\xi$ for the mixing layer with one-step reactions. All the plots are at $x/M = 50.1$ except the center right, which is at $x/M = 231$. Since the turbulence is decaying, $\langle Da_T \rangle$ is the same for the middle two panels.

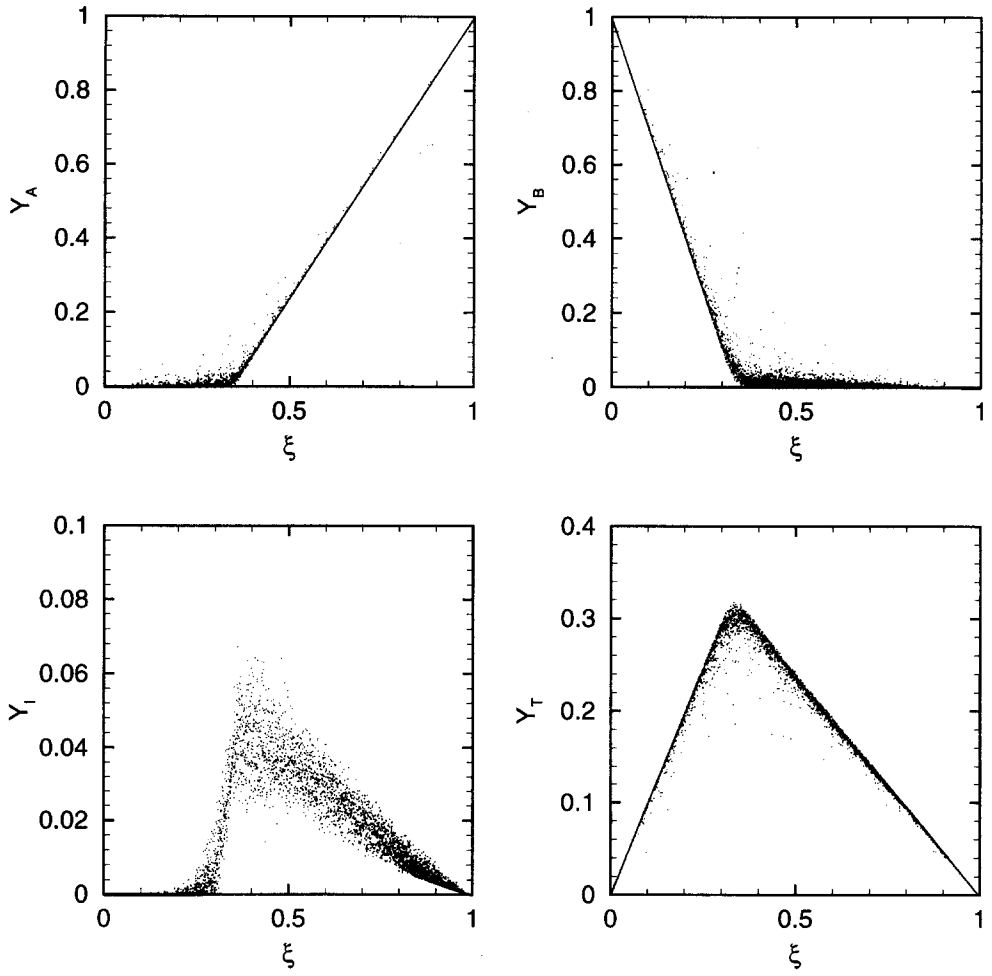


Figure 4. Scatter plots of mass fractions versus $\xi$ for the mixing layer ($x/M = 231$) with the two-step reaction.

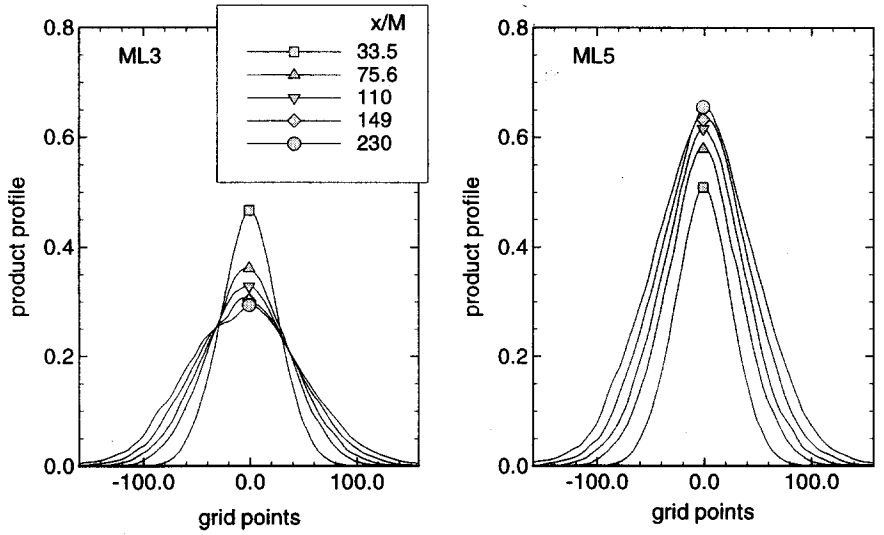


Figure 5. Product mass fraction profiles for cases M3 (left) and M5 (right).

ML4 is a nonisothermal case with intermediate reaction rate. The simulations are designed so that $\langle \mathrm{Da}_T \rangle$ is the same in ML4 at $x/M = 50.1$ and ML3 at $x/M = 231$, and is also the same in ML4 at $x/M = 231$ and ML5 at $x/M = 50.1$. So, it is possible to observe the flow at the same $\langle \mathrm{Da}_T \rangle$ but different Reynolds numbers. It is presumably easier to account for the time history of the flow on the LES models at $x/M = 231$ than at $x/M = 50.1$ since details of the initial conditions are expected to be of less consequence in the far field.

The remaining two simulations with one-step reactions (ML6 and ML7) involve temperature-dependent chemistry at a lower activation temperature than ML3 through ML5. Also, $r$ is much greater than unity so that the peak reaction rate does not coincide with the centerline of the mixing layer. Some evidence of extinction is apparent in the bottom two panels of Figure 3 for both cases, with ML7 having a less vigorous reaction than ML6.

The two-step reaction (Figure 3) is moderately fast as evidenced by the limited scatter away from the equilibrium limit of the mass fraction of fuel (species A); but there is significant scatter in the intermediate species. Even though the fuel-consuming reaction (25) proceeds near its mixing limited rate, the second reaction (26) is kinetically limited in a significant fraction of the field. Thus, the overall reaction is robust without being suitable to modelling with equilibrium methods.

## 6. QUASI-STEADY FLAMELET SOLUTIONS

The quasi-stationary flamelet (QFL) model (4) underlies the large-eddy flamelet model, and understanding the behavior of QFL is important in the understanding of LELFM. QFL has been previously examined in detail via direct numerical simulations [71–73], and a rigorous study is not repeated here. It is useful, however, to demonstrate the performance of the model when applied to the current high resolution simulations with temperature dependent kinetics; these results will be referred to in the next section in conjunction with evaluating the large-eddy laminar flamelet model.

The DNS data and QFL model predictions of product mass fractions and fuel reaction rates are shown in Figure 6 for cases where $r = 1$. The QFL results are computed by solving (4) at each point in the field using DNS results for $\xi$ and $\chi$, and assuming the $\xi$ dependence of $\chi$ given by (7). In the left-hand panels of each figure, the flamelet solutions are conditionally averaged on the DNS results, so that a straight diagonal line indicates that the model is perfect, on average, over the full range of DNS values existing in the fields. In the right-hand panels, the DNS and flamelet model results are each conditioned on the mixture fraction and averaged, thereby showing how well the model performs over the range of $\xi$. All of the plots are at $x/M = 231$, but they are typical of all downstream locations.

When the Damköhler number is low and there is considerable extinction (top panels), the QFL significantly overpredicts $Y_{\mathrm{P}}$, but underpredicts the reaction rate at this downstream location. It is expected that the QFL will overpredict the product mass fraction because the model has no mechanism for determining extinction; in this work, when an ignited solution can be found numerically for (4), it is used. In the intermediate Damköhler number case (middle panels), the QFL model yields good predictions for both the product mass fraction and the reaction rate, although it slightly underpredicts the latter over the entire range of $\dot{w}_{\mathrm{F}}$. At high Damköhler number (bottom panels), the model yields excellent predictions for the product mass fraction; the reaction rate predictions are good on average but, from the lower left-hand panel, it is evident that the model tends to underpredict the reaction rate except where the rate is extremely high.

The QFL predictions for the cases with $r > 1$ (ML6, ML7) are compared with the DNS results in Figure 7. The predictions for $Y_{\mathrm{P}}$ are excellent while, as in the cases where $r = 1$, the QFL model underpredicts $\dot{w}_{\mathrm{F}}$, especially at high values of $\dot{w}_{\mathrm{F}}$. The accurate predictions of $Y_{\mathrm{P}}$, even for Case ML7 in which the reaction rate is not particularly fast, are consistent with the finding

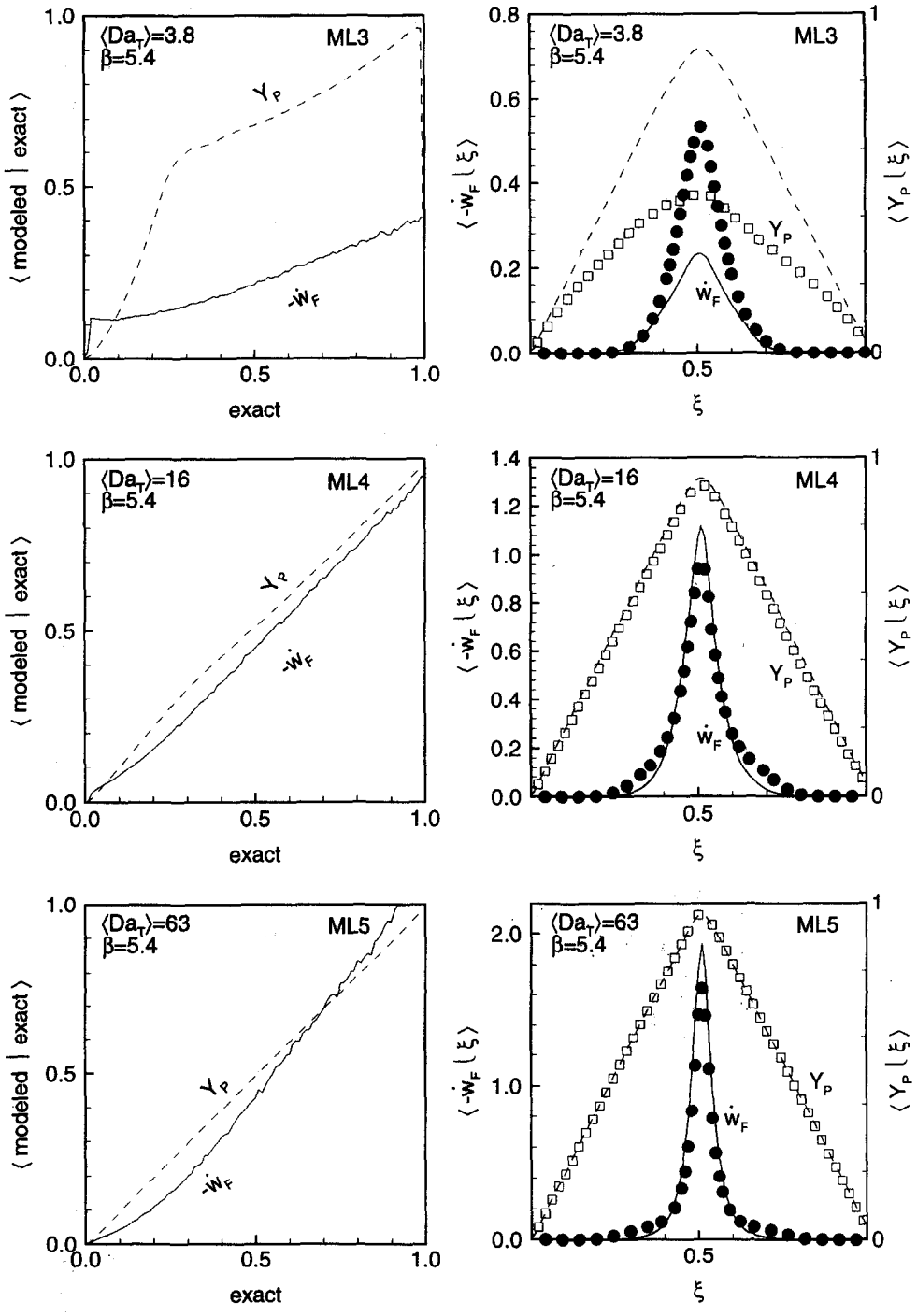


Figure 6. Two views of DNS data versus QFL predictions for product mass fractions and fuel reaction rates for cases with $r = 1$. In the right-hand plots, the symbols denote DNS results and the lines denote flamelet predictions.

of de Bruyn Kops *et al.* [22] that, with comparable global rates, reactions with $r > 1$ are easier to model than those with $r = 1$.

For the case with multistep chemistry (ML8), the QFL predictions for the mass fractions and the temperature ($Y_T$) very closely match the DNS results when conditionally averaged (Figure 8).

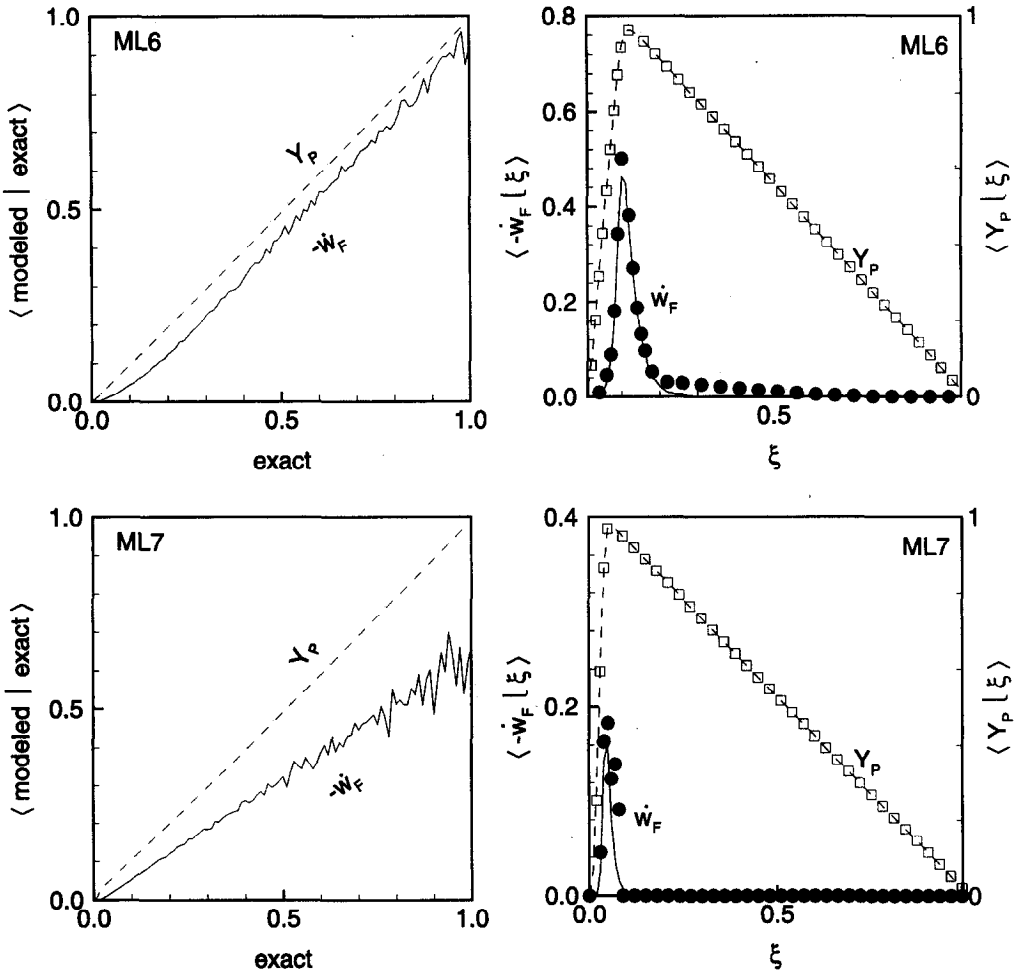


Figure 7. Two views of DNS data versus QFL predictions for product mass fractions and fuel reaction rates for cases with $r > 1$. In the right-hand plots, the symbols denote DNS results and the lines denote flamelet predictions.

This is as expected for species A and B and for the temperature, since only moderate deviation from the equilibrium limit is apparent in Figure 4. For species I, considerable deviation from quasiequilibrium is observed in many locations, so it is encouraging that the QFL predictions are very good for this species as well. As with the single-step mechanism, QFL slightly underpredicts the conditionally averaged reaction rates.

From the five single-step reaction cases examined, it is apparent that there is a tendency for QFL to underpredict $\dot{w}_F$ on average while accurately predicting the average $Y_P$ when Da is moderate to high. This characteristic is not so much a failure of the model to account for a key physical phenomenon as it is an artifact of the nonlinear nature of the Arrhenius exponential. Consider a model for $Y_P$ which is perfect on average over the full range of values, but locally has a small relative error $e$, i.e., $Y_P^{\text{model}} = Y_P(1 \pm e)$, subject to the constraint that $Y_P^{\text{model}}$ is between the frozen and equilibrium chemistry limits. Recall that for the simple reaction set considered in this work, the reduced temperature is equal to the product mass fraction. Then, when the reaction rate is computed from $Y_P^{\text{model}}$ with a small value of $e$ (less than 0.1), it will be lower than the true reaction rate computed from $Y_P$ on average, and the error will be more pronounced at higher values of $Y_P$. Libby and Williams [74] explain the phenomenon in a somewhat different manner, but either analysis leads to the conclusion that any model that accurately (on average) predicts the mass fractions, and then uses the mass fractions to estimate the reaction rate, will

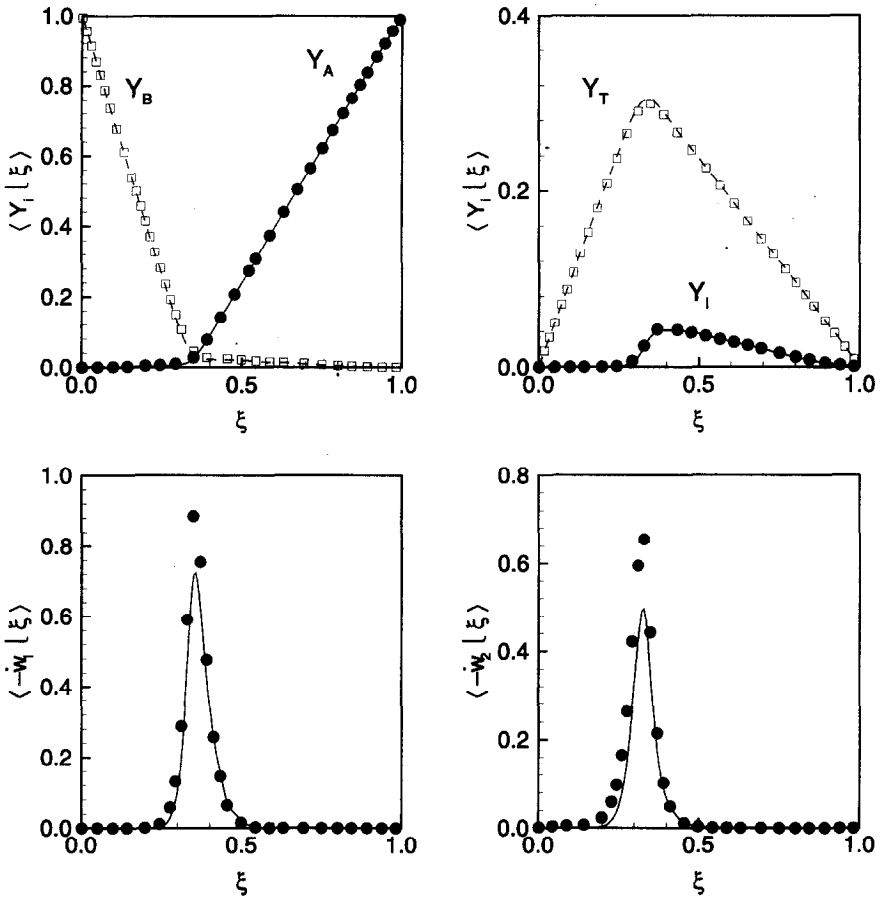


Figure 8. DNS data versus QFL predictions for mass fractions and reaction rates for the two-step reaction mechanism ($x/M = 231$). The symbols denote DNS results and the lines denote flamelet predictions.

underestimate the reaction rate when the activation temperature is high, unless the model for the mass fractions is perfect locally.

## 7. LELFM PREDICTIONS

In the previous section it was shown that the QFL model, which underlies the large-eddy laminar flamelet model, yields good predictions of the product mass fraction and fuel reaction rate in four of the five single-step reaction cases examined and in the two-step reaction case. This brief study of the QFL model serves to quantify the first of the four classes of errors that exist when the LELFM is used in conjunction with LES hydrodynamic data, namely errors in the underlying quasi-steady flamelet model. The remaining classes of errors are:

(1) errors in the LELFM model itself,
(2) errors in the submodels for $\bar{\chi}$ and $\xi_v^2$ themselves, and
(3) inaccuracies in the LES values of $\bar{\xi}$, which directly cause errors in the LELFM predictions, and which lead to errors in $\bar{\chi}$, $\xi_v^2$.

*A priori* tests on the individual components of the LELFM have been performed elsewhere: the beta PDF model [13]; LELFM with $\bar{\chi}$ and $\xi_v^2$ taken directly from the DNS [19,20,31]; and models for $\bar{\chi}$ and $\xi_v^2$ [31,33,34]. In this section, the focus is on *a posteriori* tests of the LELFM, i.e., tests of LELFM using only those inputs obtained from large-eddy simulations. The standard against which the LELFM predictions are compared is filtered DNS results; recall from Section 4 that these DNS data have been shown to closely represent wind tunnel data. We only consider the

four chemistry cases in which the QFL performed well since the LES model cannot correct errors introduced by this underlying model.

There are three quantities of primary interest in evaluating models for SGS reactions: mass fractions, temperature, and reaction rates. In reacting flows where extinction is not prevalent (e.g., vigorous combustion, reactions in the atmosphere, reactions occurring in certain chemical manufacturing processes), a useful model must be able to predict the mean mass fractions as a function of time. In flows where the reactions tend to extinguish at high rates of strain, it is presumably necessary for the SGS reaction model to be able to accurately predict the filtered temperatures and reaction rates.

### 7.1. Mass Fractions and Temperature

A principal goal of large-eddy simulations of reacting flows is to accurately predict the average concentrations of the primary species involved in the reactions. For the single-step reactions, the filtered product mass fraction is a particularly convenient quantity by which to measure the performance of the LES since it not only represents a species concentration, but it is also proportional to temperature (assuming adiabatic, unity Lewis numbers). $\langle \bar{Y}_P \mid \bar{\xi} \rangle$ from the LES is shown in Figure 9, along with the reference values computed by the filtered DNS fields, for the four cases with one-step reactions. Results using a LES numerical grid with $64^3$ points are shown since this is approximately the minimum resolution at which the velocity and scalar field subgrid-scale models yield reasonably accurate predictions [34]. The LELFM predictions of $\langle \bar{Y}_P \mid \bar{\xi} \rangle$ (using only LES results as input) are very good, and the predictions improve when the LES resolution is increased to $128^3$ grid points (not shown). This is encouraging since the LES not only yields good predictions, but the predictions approach the exact (DNS) results as the resolution is improved. It is also apparent that the LES results are consistently good at all downstream distances examined ($x/M = 43.1, 98, 231$). This characteristic of the results is encouraging, but it must be noted that:

(1) the passive scalar mixing layer is very nearly self-similar, and so time history effects on the mixing rate are minimal [21];

(2) the reacting scalars are sufficiently quasisteady that the QFL accurately predicts the conditionally averaged, unfiltered mass fractions.

The two-step reaction (ML8) provides a measure of the ability of LELFM to predict not only major species concentrations and temperature, but also intermediate species concentrations, which are important in predicting the rate of pollutant formation. In Figure 10 are shown the predicted filtered mass fractions for this case, along with the values computed by filtering the DNS results. The LELFM predictions are excellent. Comparing Figures 10 and 8, it is apparent that the additional modelling included in the LELFM to predict the filtered mass fractions from the hydrodynamic LES data and the QFL equation has a negligible effect on the predictions of the filtered mass fractions.

### 7.2. Reaction Rates

In the work discussed in this paper, the large-eddy simulations are run and the species concentrations are computed afterwards (postprocessed). To conduct large-eddy simulations of flows in which the time history of the reaction significantly affects the evolution of the flow, it is likely necessary that the reaction model accurately predicts the rates of reaction, and hence the local heat release. From Figures 6 and 8, we expected that if the LELFM is consistent with QFL, it will slightly underpredict the filtered reaction rates. Instead, when the grid resolution of the LES is $64^3$, the LELFM results in Figures 11 and 12 show that the LELFM slightly underpredicts the reaction rates at $x/M = 43.1$, and overpredicts them for larger values of $x$.

To further illustrate the characteristics of the LELFM predictions for filtered reaction rates, the QFL, LELFM, and DNS values for the reaction rates averaged over the entire computational

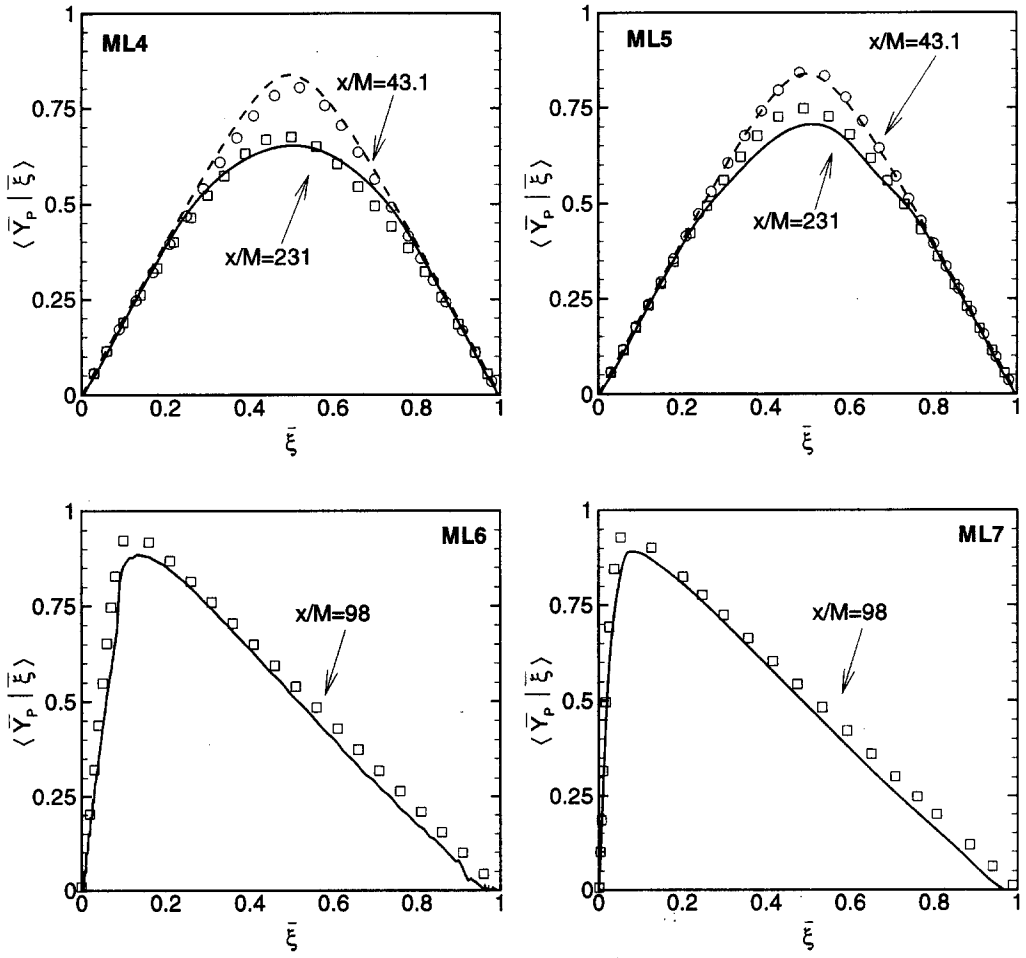


Figure 9. Filtered product mass fractions conditioned on filtered mixture fraction for the single-step mechanisms. The symbols are filtered DNS data and the lines are from the LELFM applied to $64^3$ LES data.

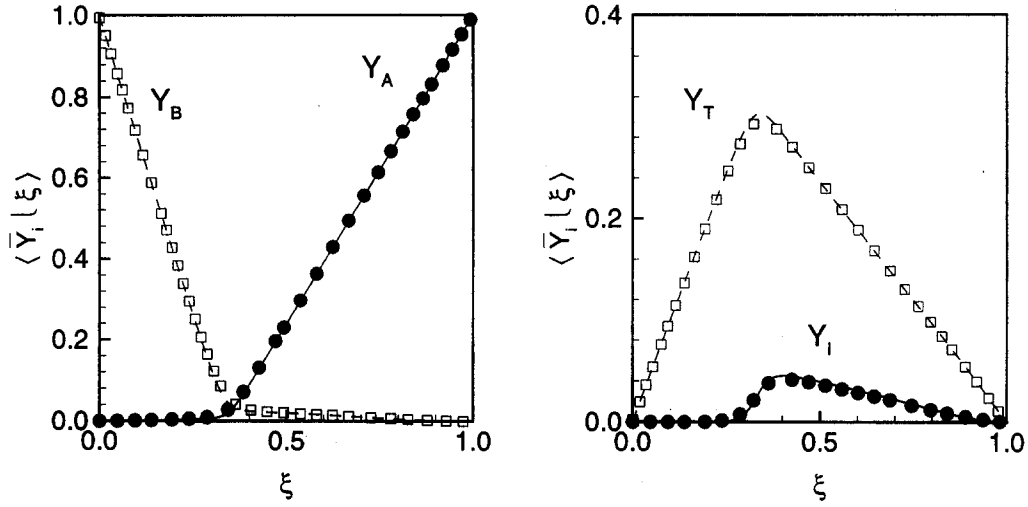


Figure 10. Filtered mass fractions conditioned on filtered mixture fraction for the two-step mechanism. The symbols are filtered DNS data and the lines are from the LELFM applied to $64^3$ LES data.

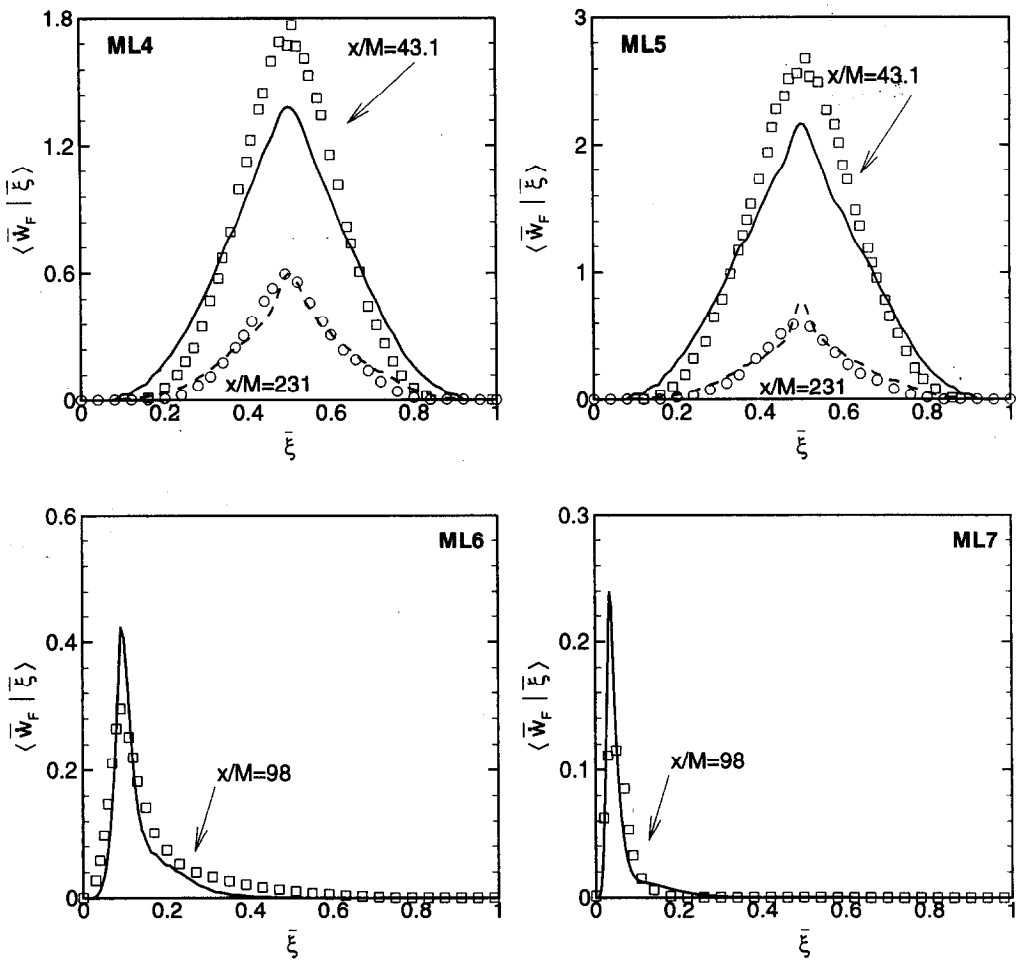


Figure 11. Filtered fuel reaction rates conditioned on filtered mixture fraction for the single-step mechanisms at $x/M = 231$. The symbols are filtered DNS data and the lines are from the LELFM applied to $64^3$ LES data ($a = 1$).

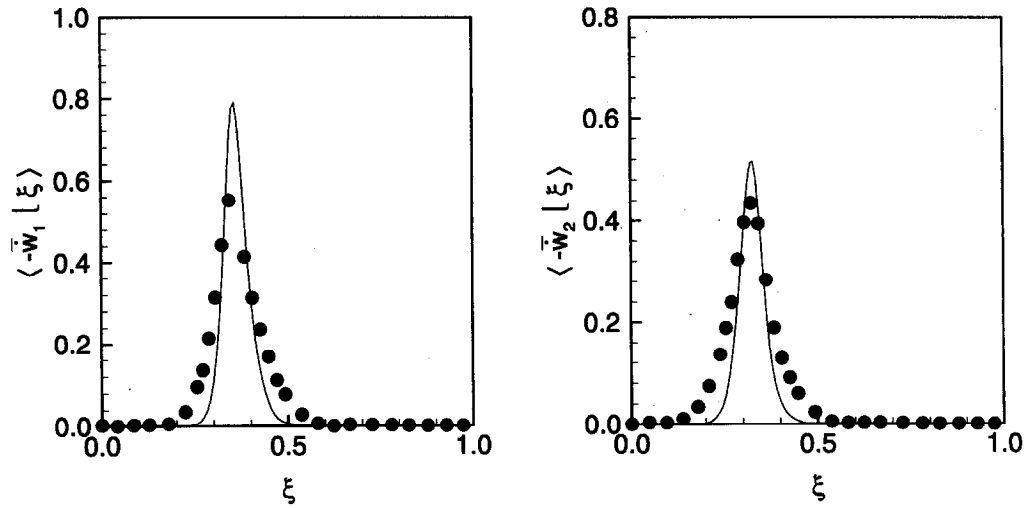


Figure 12. Filtered reaction rates conditioned on filtered mixture fraction for the two-step mechanism at $x/M = 231$. The symbols are filtered DNS data and the lines are from the LELFM applied to $64^3$ LES data ($a = 1$).

domain are given in Table 4. Consistent with the figures just referenced, LELFM tends to overpredict $\langle \bar{w}_i \rangle$ at $x/M = 231$ when the LES grid spacing is relatively coarse; even in the cases in which the LELFM prediction is less than the DNS result, it still exceeds the QFL prediction. When the LES resolution is increased to $128^3$-points, the LELFM predictions approach the QFL results.

Table 4. Predictions of $\langle \bar{w}_i \rangle$ as a fraction of the DNS values. The symbol $a$ is that in (14).

| | | $x/M$ | QFL | $64^3$ LES | | $128^3$ LES | |
|---|---|---|---|---|---|---|---|
| | | | | $a = 0$ | $a = 1$ | $a = 0$ | $a = 1$ |
| ML4 | $\langle \bar{w}_F \rangle$ | 43 | 0.82 | 1.20 | 0.98 | 1.13 | 0.92 |
| ML4 | $\langle \bar{w}_F \rangle$ | 231 | 0.96 | 1.25 | 1.04 | 1.12 | 0.93 |
| ML5 | $\langle \bar{w}_F \rangle$ | 43 | 0.88 | 1.12 | 0.94 | 1.07 | 0.89 |
| ML5 | $\langle \bar{w}_F \rangle$ | 231 | 1.10 | 1.28 | 1.14 | 1.18 | 1.05 |
| ML6 | $\langle \bar{w}_F \rangle$ | 98 | 0.78 | 0.82 | 0.73 | 0.90 | 0.79 |
| ML7 | $\langle \bar{w}_F \rangle$ | 98 | 0.87 | 1.07 | 0.93 | 1.33 | 0.90 |
| ML8 | $\langle \bar{w}_1 \rangle$ | 231 | 0.82 | 0.96 | 0.92 | 0.95 | 0.86 |
| ML8 | $\langle \bar{w}_2 \rangle$ | 231 | 0.71 | 0.87 | 0.82 | 0.91 | 0.78 |

In (14), the parameter $a$ is used to relate the mean and the variance of the SGS $\xi$ when the PDF of that quantity is modelled with a lognormal distribution. The effect of varying $a$ between 0 and 1 is evident in Table 4. When $a = 0$, the LELFM predictions significantly exceed those of the QFL, indicating that modelling the SGS $\chi$ with a Dirac delta function introduces errors into the model for the filtered mass fractions that counteract the errors in the underlying QFL model. When $a = 1$, the LELFM results more closely agree with the QFL predictions. While this does not prove that the one-parameter logarithmic distribution for SGS $\chi$ is appropriate, it is encouraging. Furthermore, for most of the cases considered, the LELFM results with $128^3$-point resolution and $a = 1$ very nearly agree with the QFL results.

## 8. CONCLUSIONS

The large-eddy laminar flamelet model (LELFM) is one of several approaches to modelling reactions that occur at length scales smaller than those resolved on an LES numerical grid. The model is based on the quasi-steady flamelet (QFL) model and requires as input the filtered mean and variance of the mixture fraction, as well as its filtered dissipation rate; the first of these quantities is computed directly from an evolution equation in an LES, while the latter two are modelled in the present study. Validations of all of the elements of the LELFM have been previously reported [13,19,20,31,33,34]. Presented in this paper are the results of integrated tests of the LELFM in which mass fractions, temperatures, and reaction rates, computed using only LES data as input, are compared with benchmark results from high resolution DNS. The benchmark data includes single- and two-step reaction mechanisms with a range of stoichiometric ratios and activation temperatures, and, based on results shown elsewhere [21,22], are expected to accurately represent passive reactions superimposed on the wind tunnel experiments of Ma and Warhaft [63].

Examined are six chemistry cases, five of which are shown to be suitable for modelling with the QFL approach; the sixth is included to emphasize that the LELFM, since it is based on QFL, is not appropriate for modelling reactions in which QFL does not apply. For the five cases in which the QFL model yields good results for the unfiltered mass fractions, the following conclusions about the performance of the LELFM for predicting filtered mass fractions, reaction rates, and temperatures can be drawn:

(1) the LELFM yields excellent predictions for filtered mass fractions and temperatures;

(2) the LELFM yields good predictions for filtered reaction rates, even when the reaction is much thinner than the LES grid spacing;
(3) the additional modelling (beyond that in the QFL model) involved in the LELFM approach has a negligible effect on the results of the model;
(4) LELFM predictions of filtered reaction rates are more consistent with QFL predictions of the corresponding unfiltered quantities when a lognormal PDF is assumed for the SGS dissipation rate than when a Dirac delta function PDF is assumed.

The LELFM is presently applicable to a wide range of nonpremixed combustion problems, and the current results encourage the thought that advances that broaden the applicability of flamelet modelling will carry over to the LELFM.

## REFERENCES


1. N. Branley and W.P. Jones, Large eddy simulation of a turbulent non-premixed flame, In *Proceedings of the $11^{th}$ Symposium on Turbulent Shear Flows*, Grenoble, France, pp. 21.1–21.6, (1997).
2. P.J. Colucci, F.A. Jaberi, P. Givi and S.B. Pope, Filtered density function for large eddy simulation of turbulent reacting flows, *Phys. Fluids* **10** (2), 499–515, (1998).
3. C. Fureby, E. Lundgren and S.I. Moller, Large-eddy simulations of bluff body stabilized flames, In *$25^{th}$ Symposium (International) on Combustion*, Combustion Institute, Pittsburgh, PA, pp. 1257–1264, (1994).
4. P. Givi, Model free simulations of turbulent reactive flows, *Prog. Energy Combust. Sci.* **15**, 1–107, (1989).
5. T.M. Liou, W.Y. Lien and P.W. Hwang, Large-eddy simulations of turbulent reacting flows in chamber with gaseous ethylene injecting through the porous wall, *Combust. Flame* **99**, 591–600, (1994).
6. P.A. McMurtry, S. Menon and A.R. Kerstein, A linear eddy sub-grid model for turbulent reacting flows: Application to hydrogen-air combustion, In *Twenty-Fourth Symposium (International) on Combustion*, The Combustion Institute, Pittsburgh, PA, pp. 271–278, (1992).
7. U. Schumann, Large eddy simulation of turbulent diffusion with chemical reactions in the convective boundary layer, *Atmos. Environ.* **23** (8), 1713–1727, (1989).
8. R.I. Sykes, D.S. Henn, S.F. Parker and W.S. Lewellen, Large-eddy simulations of a turbulent reacting plume, *Atmos. Environ. A* **26** (14), 2565–2574, (1992).
9. F. Gao and E.E. O'Brien, A large-eddy simulation scheme for turbulent reacting flows, *Phys. Fluids A* **5**, 1282–1284, (1993).
10. R.W. Bilger, Turbulent flows with nonpremixed reactants, In *Topics in Applied Physics Number 44: Turbulent Reacting Flows*, (Edited by P.A. Libby and F.A. Williams), Chapter 3, pp. 65–113, Springer-Verlag, New York, (1980).
11. D. Lentini, Assessment of the stretched laminar flamelet approach for non-premixed turbulent combustion, *Combust. Sci. Technol.* **100**, 95–122, (1994).
12. S.H. Frankel, V. Adumitroaie, C.K. Madnia and P. Givi, Large-eddy simulation of turbulent reacting flows by assumed PDF methods, In *Engineering Applications of Large Eddy Simulations*, pp. 81–101, ASME, New York, (1993).
13. A.W. Cook and J.J. Riley, A subgrid model for equilibrium chemistry in turbulent flows, *Phys. Fluids* **6** (8), 2868–2870, (1994).
14. F.A. Jaberi and S. James, A dynamic similarity model for large eddy simulation of turbulent combustion, *Phys. Fluids* **10** (7), 1775–1777, (1998).
15. N. Peters, Laminar diffusion flamelet models in non-premixed turbulent combustion, *Prog. Energy Combust. Sci.* **10**, 319–339, (1984).
16. Yu.Ya. Buriko, V.R. Kuznetsov, D.V. Volkov, S.A. Zaitsev and A.F. Uryvsky, A test of a flamelet model for turbulent nonpremixed combustion, *Combust. Flame* **96**, 104–120, (1994).
17. H. Pitsch, M. Chen and N. Peters, Unsteady flamelet modeling of turbulent hydrogen/air diffusion flames, In *$27^{th}$ Symposium (International) on Combustion*, Combustion Institute, Pittsburgh, PA, p. 1057, (1998).
18. J.P.H. Sanders, J.-Y. Chen and I. Gökalp, Flamelet based modeling of NO formation in turbulent hydrogen jet diffusion flames, *Combust. Flame* **111**, 1–15, (1997).
19. A.W. Cook, J.J. Riley and G. Kosály, A laminar flamelet approach to subgrid-scale chemistry in turbulent flows, *Combust. Flame* **109**, 332–341, (1997).
20. A.W. Cook and J.J. Riley, Subgrid-scale modeling for turbulent, reacting flows, *Combust. Flame* **112**, 593–606, (1997).
21. S.M. de Bruyn Kops and J.J. Riley, Re-examining the thermal mixing layer with numerical simulations, *Phys. Fluids* **12** (1), 185–192, (2000).
22. S.M. de Bruyn Kops, J.J. Riley and G. Kosály, Direct numerical simulation of reacting scalar mixing layers, *Phys. Fluids* **3** (5), 1450–1465, (2001).
23. U. Piomelli, Large-eddy simulation: Achievements and challenges, *Progress in Aerospace Sciences* **35** (4), 335–362, (May 1999).
24. C. Meneveau and J. Katz, Scale-invariance and turbulence models for large-eddy simulations, *Annu. Rev. Fluid Mech.* **32**, 1–32, (2000).

25. J. Smagorinsky, General circulation experiments with the primitive equations. I. The basic experiment, *Mon. Weather Rev.* **91**, 99–164, (1963).
26. D.K. Lilly, The representation of small-scale turbulence in numerical simulation experiments, In *Proc. IBM Scientific Computing Symp. Environ. Sci.*, p. 195, (1967).
27. M. Germano, U. Piomelli, P. Moin and W.H. Cabot, A dynamic subgrid-scale eddy viscosity model, *Phys. Fluids A* **3**, 1760–1765, (1991).
28. M. Germano, Turbulence: The filtering approach, *J. Fluid Mech.* **238**, 325–336, (1992).
29. D. Carati, S. Ghosal and P. Moin, On the representation of backscatter in dynamic localization models, *Phys. Fluids* **7** (3), 606–616, (1995).
30. D.K. Lilly, A proposed modification of the Germano subgrid-scale closure method, *Phys. Fluids A* **4**, 633–635, (1992).
31. S.M. de Bruyn Kops, J.J. Riley, G. Kosály and A.W. Cook, Investigation of modeling for non-premixed turbulent combustion, *Flow. Turb. and Comb.* **60** (1), 105–122, (1998).
32. S.M. de Bruyn Kops, Numerical simulation of non-premixed turbulent combustion, Ph.D. Thesis, University of Washington, (1999).
33. S.M. de Bruyn Kops and J.J. Riley, Large-eddy simulation of non-premixed turbulent combustion, In *Proceedings of 1999 ASME/JSME Fluids Engineering Division Summer Meeting*, (1999).
34. S.M. de Bruyn Kops and J.J. Riley, Mixing models for large-eddy simulation of non-premixed turbulent combustion, *Journal of Fluids Engineering* **123** (2), 341–346, (2001).
35. K.A. Buch and W.J.A. Dahm, Experimental-study of the fine-scale structure of conserved scalar mixing in turbulent shear flows. Part I: Sc $\gg$ 1, *J. Fluid Mech.* **317**, 21–71, (1996).
36. G.R. Ruetsch and M.R. Maxey, Small-scale features of vorticity and passive scalar fields in homogeneous isotropic turbulence, *Phys. Fluids A* **3** (6), 1587–1597, (June 1991).
37. E.D. Siggia, Numerical study of small-scale intermittency in three-dimensional turbulence, *J. Fluid Mech.* **107**, 375–406, (1981).
38. K.B. Southerland and W.J.A. Dahm, A four-dimensional experimental study of conserved scalar mixing in turbulent flows, Report No. 026779-12, The University of Michigan, Ann Arbor, MI, (1994).
39. C.H. Gibson and P.A. Libby, On turbulent flows with fast chemical reactions. Part II. The distribution of reactants and products near a reaction surface, *Combust. Sci. Technol.* **6**, 29–35, (1972).
40. V.R. Kuznetsov and V.A. Sabel'nikov, *Turbulence and Combustion*, Hemisphere, New York, (1990).
41. F.A. Williams, *Combustion Theory: The Fundamental Theory of Chemically Reacting Flow Systems*, Second Edition, Benjamin-Cummings, Menlo Park, CA, (1985).
42. A.W. Cook, On the simulation and modeling of turbulent reacting flows, Ph.D. Thesis, University of Washington, (1996).
43. A.R. Kerstein and W.T. Ashurst, Lognormality of gradients of diffusive scalars in homogeneous, two-dimensional mixing systems, *Phys. Fluids* **27**, 2819–2827, (1984).
44. F. Anselmet and R.A. Antonia, Joint statistics between temperature and its dissipation in a turbulent jet, *Phys. Fluids* **28**, 1048–1054, (1985).
45. V. Eswaran and S.B. Pope, Direct numerical simulations of the turbulent mixing of a passive scalar, *Phys. Fluids* **31**, 506, (1988).
46. A. Pumir, A numerical study of the mixing of a passive scalar in three dimensions in the presence of a mean gradient, *Phys. Fluids* **6**, 2118–2132, (1994).
47. M. Holzer and E.D. Siggia, Turbulent mixing of a passive scalar, *Phys. Fluids* **6**, 1820–1837, (1994).
48. J. Jiménez, A. Liñán, M.M. Rogers and F.J. Higuera, *A priori* testing of sub-grid models for chemically reacting nonpremixed turbulent shear flows, *J. Fluid Mech.* **349**, 149–171, (1997).
49. C. Jiménez, F. Ducros and B. Cuenot, Subgrid scale variance and dissipation of a scalar field in large eddy simulation combustion models, In *8th European Turbulence Conference*, Barcelona, Spain, (2000).
50. A. Yoshizawa, Statistical theory for compressible turbulent shear flows, with the application to subgrid modeling, *Phys. Fluids A* **29**, 2152–2164, (1986).
51. F. Mathey and J.P. Chollet, Sub-grid model of scalar mixing for large eddy simulations of turbulent flows, In *The Second ERCOFTAC Workshop on Direct and Large Eddy Simulations*, Grenoble, France, (1996).
52. A.W. Cook, Determination of the constant coefficient in scale similarity models of turbulence, *Phys. Fluids* **9** (5), 1485–1487, (1997).
53. S. Corrsin, Further generalization of Onsager's cascade model for turbulent spectra, *Phys. Fluids* **7**, 1156, (1964).
54. Y.H. Pao, Statistical behavior of a turbulent multicomponent mixture with first order reactions, *AIAA J.* **2**, 1550, (1964).
55. Y.H. Pao, Structure of turbulent velocity and scalar fields at large wavenumbers, *Phys. Fluids* **8** (6), 1063–1075, (1965).
56. J.O. Hinze, *Turbulence*, Second Edition, McGraw-Hill, New York, (1975).
57. S.S. Girimaji and Y. Zhou, Analysis and modeling of subgrid scalar mixing using numerical data, *Phys. Fluids A* **8** (5), 1224–1236, (1996).
58. A.W. Cook, Modeling $\tilde{\chi}$, Private Communication, (1997).
59. A. Liñán, The asymptotic structure of counterflow diffusion flames for large activation energies, *Acta Astron.* **1**, 1007, (1974).

60. B. Cuenot and T. Poinsot, Effects of curvature and unsteadiness in diffusion flames. Implications for turbulent diffusion combustion, In *25$^{th}$ Symposium (International) on Combustion*, Combustion Institute, Pittsburgh, PA, pp. 1383–1390, (1994).
61. B. Cuenot and T. Poinsot, Asymptotic and numerical study of diffusion flames with variable Lewis number and finite rate chemistry, *Combust. Flame* **104**, 111–137, (1996).
62. N. Swaminathan and R.W. Bilger, Direct numerical simulation of turbulent nonpremixed hydrocarbon flames using a two-step reduced mechanism, *Combustion Science and Technology* **127** (1–6), 167–196, (1997).
63. B.-K. Ma and Z. Warhaft, Some aspects of the thermal mixing layer in grid turbulence, *Phys. Fluids* **29** (10), 3114–3120, (1986).
64. S.M. de Bruyn Kops and J.J. Riley, Direct numerical simulation of laboratory experiments in isotropic turbulence, *Phys. Fluids* **10** (9), 2125–2127, (1998).
65. G. Comte-Bellot and S. Corrsin, Simple Eulerian time correlation of full and narrow-band velocity signals in grid-generated, 'isotropic' turbulence, *J. Fluid Mech.* **48**, 273–337, (1971).
66. D. Gottlieb and S.A. Orszag, Numerical analysis of spectral methods: Theory and applications, *Volume 26*, In *NSF-CBMS, Regional Conference Series in Applied Mathematics*, Society of Industrial and Applied Mathematics, Philadelphia, PA, (1977).
67. P. Peyret and T.D. Taylor, *Computational Methods for Fluid Flows*, Springer-Verlag, New York, (1983).
68. S.A. Orszag and G.S. Patterson, Numerical simulation of turbulence, In *Statistical Models and Turbulence*, Volume 12 of Lecture Notes in Physics, (Edited by J. Ehlers, K. Hepp and H.A. Weidenmüller), pp. 127–147, Springer, New York, (1972).
69. C. Canuto, M.Y. Hussaini, A. Quarteroni and T.A. Zang, *Spectral Methods in Fluid Dynamics*, Springer, New York, (1988).
70. P.A. McMurtry, Direct numerical simulations of a reacting mixing layer with chemical heat release, Ph.D. Thesis, University of Washington, (1987).
71. W.E. Mell, C. Nilsen, G. Kosály and J.J. Riley, Investigation of closure models for turbulent reacting flow, *Phys. Fluids A* **6**, 1331–1356, (1994).
72. W.E. Mell, An investigation of closure models for nonpremixed turbulent reacting flow, Ph.D. Thesis, University of Washington, (1994).
73. S.M. de Bruyn Kops, G. Kosály and J.J. Riley, Investigation of the flamelet modeling of turbulent combustion, Technical Report GRI-97/0031, Gas Research Institute, Chicago, IL, (March 1997).
74. P.A. Libby and F.A. Williams, *Turbulent Reacting Flows, Volume 44*, Chapter 1, pp. 1–43, Springer, Berlin, (1980).